Strain Accumulation and Release of the Gorkha, Nepal, Earthquake (M_w 7.8, 25 April 2015)

FEDERICO MORSUT,[1] TOMMASO PIVETTA,[1] CARLA BRAITENBERG,[1] and GIORGIO PORETTI[1]

Abstract—The near-fault GNSS records of strong-ground movement are the most sensitive for defining the fault rupture. Here, two unpublished GNSS records are studied, a near-fault-strong-motion station (NAGA) and a distant station in a poorly covered area (PYRA). The station NAGA, located above the Gorkha fault, sensed a southward displacement of almost 1.7 m. The PYRA station that is positioned at a distance of about 150 km from the fault, near the Pyramid station in the Everest, showed static displacements in the order of some millimeters. The observed displacements were compared with the calculated displacements of a finite fault model in an elastic halfspace. We evaluated two slips on fault models derived from seismological and geodetic studies: the comparison of the observed and modelled fields reveals that our displacements are in better accordance with the geodetic derived fault model than the seismologic one. Finally, we evaluate the yearly strain rate of four GNSS stations in the area that were recording continuously the deformation field for at least 5 years. The strain rate is then compared with the strain released by the Gorkha earthquake, leading to an interval of 235 years to store a comparable amount of elastic energy. The three near-fault GNSS stations require a slightly wider fault than published, in the case of an equivalent homogeneous rupture, with an average uniform slip of 3.5 m occurring on an area of 150 km × 60 km.

1. Introduction

The Gorkha district (Nepal) was struck on the 25th of April 2015 by a 7.8 M_w earthquake that caused over 8000 victims, over 20,000 injured and destroyed several villages and cities in the Kathmandu area. The earthquake occurred in one of the most tectonically active areas of the Earth, where the collision between the Indian and Eurasia plates generates several seismic sources, capable of catastrophic earthquakes up to 8 M_w (Z12 zone of Chaulagain et al. 2015; Rajendran and Rajendran 2011). The superficial effect of this earthquake was

recorded by different geodetic and seismological networks spread over the whole Nepal area: in particular, several continuous GNSS stations were active in the surrounding of the epicenter during the earthquake. For this reason and obviously for the terrible impact on the population and human activities, the Gorkha earthquake was widely studied (Avouac et al. 2015; Galetzka et al. 2015; Grandin et al. 2015; Sreejith et al. 2016; Arora et al. 2017).

Galetzka et al. (2015) performed an analysis on GNSS (Global Navigation Satellite System) and InSar (Interferometic Synthetic Aperture Radar) interferometry data which were jointly inverted to retrieve the spatial distribution of the slip on the fault. Similarly, Wang and Fialko (2015) performed an inversion of geodetic data, investigating different assumptions of the fault geometries. Galetzka et al. (2015) additionally derived from the continuous GNSS time series and the teleseismic records a model for the slip rate release on the earthquake, providing a kinematic model of the rupture. Grandin et al. (2015) included strong-motion data, teleseismic, high rate GNSS, and InSAR in a joint inversion scheme to gain insights into the whole rupture process. The inverted slip pattern is in accordance with Galtezka et al. (2015), but seems a little greater in certain zones. Avouac et al. (2015) analyze teleseismic records and SAR images to study the earthquake in terms of nucleation and rupture process. Sreejith et al. (2016) analyzed coseismic and post-seismic deformations from a combination of GNSS and InSAR observations. They consider the fault to be constituted by a combination of flat and a ramp structure; the authors inverted for both coseismic and post-seismic deformations. The retrieved fault slip model agrees with Galetzka et al. (2015) in terms of both magnitude and direction. The difference between observation and calculation reported in the contribution evidences a

[1] Department of Mathematics and Geosciences, University of Trieste, Via Weiss 1, Trieste, Italy. E-mail: tpivetta@units.it

slight underestimation of the GNSS data. For this model, the coseismic slip occurred prevalently on the ramp, while the post-seismic slip involved the northern sector along the flat structure. Denolle et al. (2015) studied the dynamics of the event by computing P wave spectra. Fan and Shearer (2015), from the analysis of teleseismic P waves, revealed that the earthquake was an almost unilateral rupture that propagated in the east–west direction with a rupture length of 165 km. Supplementary GNSS stations were also added immediately after the main shock, to monitor the post-seismic fault movements. Gualandi et al. (2016) and Mencin et al. (2016) testified the presence of a post-seismic afterslip that released an aseismic moment equivalent of 7.1 M_w (Mencin et al. 2016).

Arora et al. (2017) analyze the time space pattern of aftershock activity and find evidence for high pore pressure fluid fluxes into the crust.

Regarding the coseismic slip, the contributions, although diverging regarding the assumptions on the physical model, revealed that the slip occurred on a 150 km × 50-km portion of the fault that gently dips towards North–North-East (azimuth 290°E from N, dip 8–10°) and constitutes an important fault of the Main Himalayan Thrust. The extent of the fault area is in accordance also with the distribution and location of the aftershocks. According to the focal mechanism solution from seismology, the earthquake is almost a pure compressional event (USGS).

The scientific group EverestK2 (EvK2), in collaboration with the CNR (Italian National Council of Research), placed a continuous GNSS station (PYRA) in 2009 next to the Pyramid Laboratory in the Everest Mountain. Another one was placed in Nagarkot (NAGA) near Kathmandu, in Nepal. Both stations were programmed to sample the position every 30 s; from 2014, both the time series present gaps in the data, due to logistic problems in the data management which occurred during this period.

Fortunately, the stations were active in the area in the period from March 2015 to October 2015; hence, they were able to record the geodetic effect of the Gorkha earthquake and also the relevant 7.3 M_w aftershock which occurred in May 2015. The NAGA station is above the fault, increasing the near-fault observation from two to three stations. Our station

confirms that the models underestimate the dislocation in the near field.

In this contribution, we present the elaboration of the GNSS time series from the 23rd to the 26th April 2015 and a comparison with other geodetic data available for the area. We also tried to verify the compatibility of our coseismic superficial deformation with the predicted deformation calculated from a fault model, using the Okada dislocation model in an elastic halfspace (Okada 1985).

Finally, we present an analysis on the recurrence time of the earthquake in the area based on the comparison of the strain released by the Gorkha fault and the interseismic strain rate estimated from other long period GNSS time series. The work contributes in demonstrating the usefulness of the geodetic measurements in defining the strain accumulation and release during the seismic cycle, which is an important aspect for the characterization of the seismic risk of an area.

2. GNSS Elaboration

To process our GNSS data from PYRA and NAGA stations, we used 30 s sample RINEX files for both of them, as well as other files for the Bernese Software 5.2 like various Center for Orbit Determination in Europe (CODE) products for raw corrections (satellite ephemerides, Earth parameters, clock bias corrections, ionosphere parameters, and infra-code biases). For a very precise position, we need also the Vienna Mapping Function 1 parameters (VMF1, Böhm et al. 2006), used to mitigate tropospheric errors.

The first step consisted in calculating station positions precisely, in fact using the precise point position technique (PPP-PPP_VMF1.PCF script), by which it is possible to determine the absolute position of our stations in the ITRF 2008 system. As another useful result, we estimated a first plate velocity (Eurasian and Indian for both stations). During this step, we also calculated other station positions to realize a second more precise estimation of positions: the Lhasa (LHAZ) and Kitab (KIT3) stations belonging to the IGS (International GNSS Service) Network.

The second step consisted in using the double-difference technique (DD-RNX2SNX_VMF1.PCF) with a kinematic approach, where we have a position estimation for every sample (every 30 s). This approach is more precise than PPP; in fact, we can have a millimeter precision.

The time series of displacements of our stations were estimated from double-difference solutions using a kinematic approach. The locations of the two stations are presented in Table 1. In Fig. 2, we present the three components (N, E, and U) in UTM 45 R from original Bernese Earth Centered, Earth Fixed (ECEF) coordinates. We analyzed 3 days from 24th to 26th of April 2015. The two stations have been analyzed thus with the same procedure, that is first with the PPP procedure, and then with the double difference. The millimetric noise level is similar to the two stations, but the different scales used in Figs. 1 and 2 for illustrating the time series are very different, due to the fact that the dislocation is over 1 m in NAGA, and at centimetric level in PYRA.

3. GNSS Data Analysis: Comparison Between Modelled and Observed Coseismic Data

The NAGA station clearly detected on all the three components of the coseismic surface displacement, as is evident from Fig. 1. The station is close to

other two GNSS stations used by Galetzka et al. (2015) to retrieve the slip on the fault: magnitude and direction of the displacement are in agreement with those stations. With our station, the near-fault coseismic movement has been detected by three stations, increasing the number of near-fault observations. The observation of the new station with a movement in the southern direction (1.76 m) and an uplift of almost 1.2 m is coherent with the existing stations, allowing a robust estimate of the coseismic displacement. In the next 36 h, other three greater 6 M_w events occurred according to USGS catalogue (6.1 M_w, 25/04/2015 at 06:15:22; 6.6 M_w, 25/04/2015 at 06:45:21; and 6.7 M_w, 26/04/2015 at 07:09:10); however, no coseismic displacement has been produced.

The PYRA station (Fig. 2) shows instead a slighter displacement: the effect of the earthquake is more visible on the North (2 cm) component with respect to the East (1 cm). The up/down movement seems to be absent, but could be masked by the higher noise on the height component.

As already stated, GNSS time series acquired at high sampling rates requires precise removing of the atmospheric effects to not alter the tectonic signal. In particular, in these mountainous areas, snow precipitation that accumulates on the top of the GNSS antenna could significantly introduce errors in the positioning system.

To exclude the influence of rapid changes in the atmospheric conditions, not modelled by the VMF1 corrections, we plot temperature, pressure, and snow level for the PYRA station, next to the observed time series. The data were obtained from a CNR meteorological station placed near the GNSS station. All the data have been down sampled from the original 1 s to a 30 s sampling after an anti-alias filter was applied. As is evident from Fig. 2, no clear correlation exists between the deformation time series and the atmospheric conditions. Calculating the Pearson coefficient between each component of displacement and pressure and temperature time series, we obtain values ranging between 0.08 and 0.12 testifying scarce influence of the atmospheric variables and displacement. We calculated the Pearson coefficient also for the GNSS-filtered time series, with a 51 point running average, which minimizes the high-

Table 1

Location of the GNSS stations analyzed in this study. The first ten stations were considered also in Galetzka et al. (2015)

#	Name	Latitude (°)	Longitude (°)
1	DNGD	28.754	80.582
2	DNSG	28.345	83.763
3	JMSM	28.805	83.743
4	KKN4	27.801	85.279
5	NAST	27.657	85.328
6	NPGJ	28.117	81.595
7	PYUT	28.101	82.987
8	RMTE	26.991	86.597
9	SMKT	29.969	81.807
10	TPLJ	27.352	87.710
11	PYRA	27.957	86.815
12	NAGA	27.693	85.521

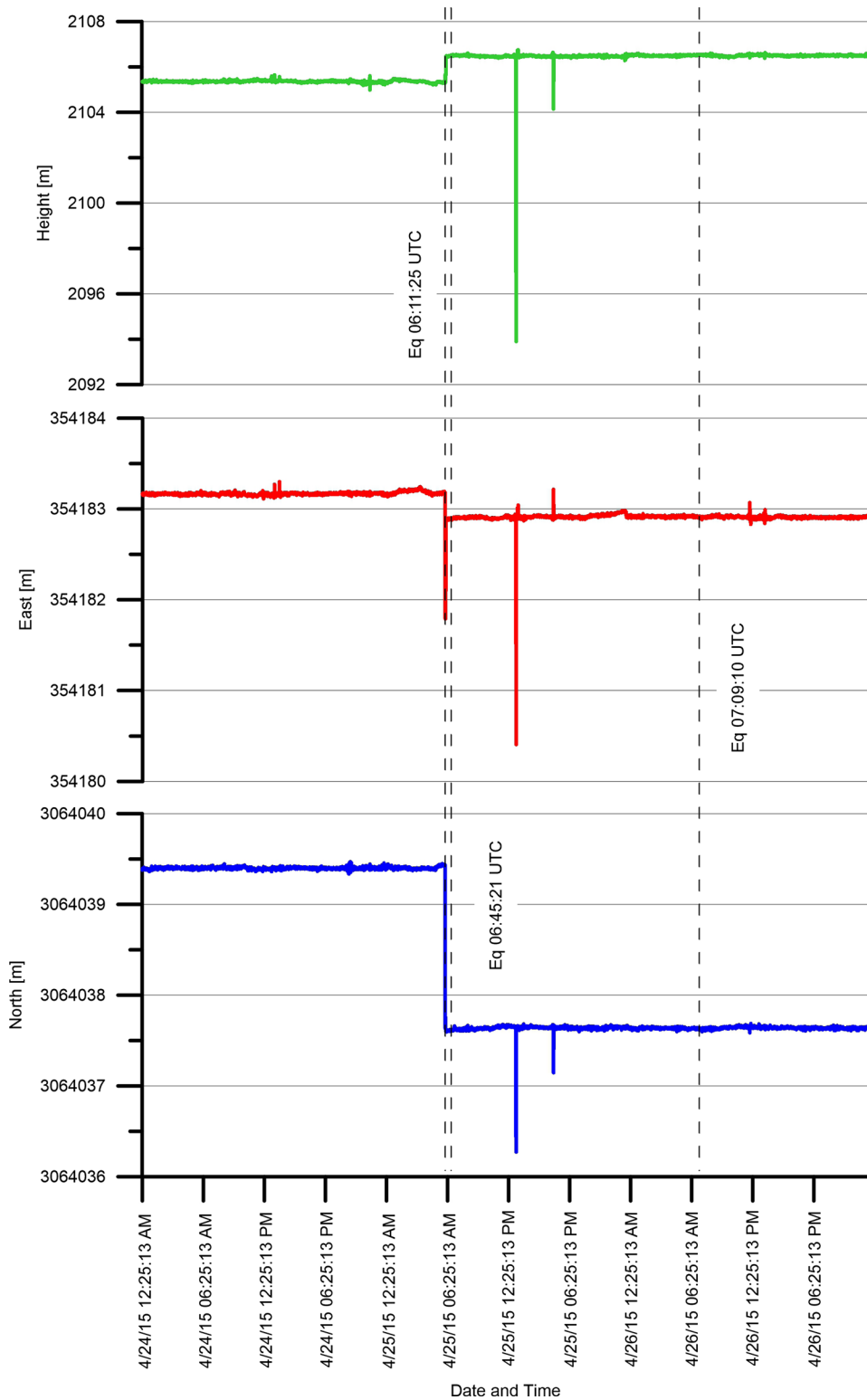The last two are the new stations, which are presented in detail in the following

Figure 1
Displacement time series of the three components observed at NAGA station from the 24th to the 26th of April. The earthquake and aftershock ($M_w > 6$) occurrence times are marked as *bold vertical dashed lines*
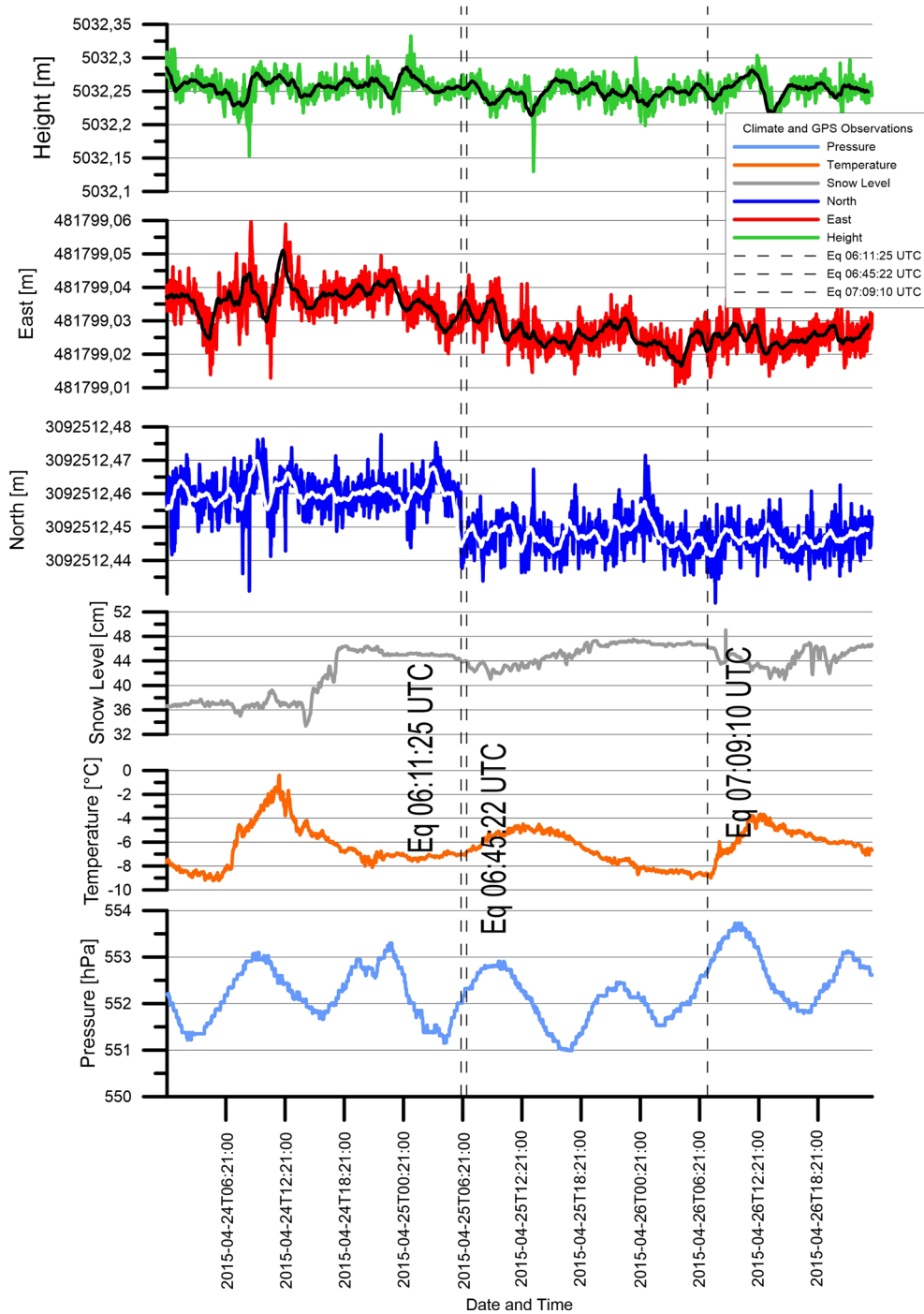
Figure 2
Displacement time series of the three components observed at the PYRA station from the 24th to the 26th of April 2015 reported together with the filtered time series, with a 51 points running average (*black* and *white lines*). The earthquake time is marked as *vertical dashed line*. Temperature, snow level, and pressure are also plotted. The meteorological data are courtesy of EvK2-CNR Pyramid Laboratory. As is evident, no correlation exists between the time series and the atmospheric parameters

Table 2

Summary of the position statistics before and after the Gorkha earthquake for NAGA and PYRA stations

PYRA	North (m)	RMS (m)	East (m)	RMS (m)	Height (m)	RMS (m)
24/04/2015	3092512.46151	0.00049	481799.03685	0.00056	5032.25657	0.00220
26/04/2015	3092512.44653	0.00044	481799.02426	0.00051	5032.25448	0.00198
Delta	−0.01498	0.00066	−0.01259	0.00076	−0.00209	0.00296
NAGA	North (m)	RMS (m)	East (m)	RMS (m)	Height (m)	RMS (m)
24/04/2015	3064039.39881	0.00052	354183.16418	0.00063	2105.35817	0.00236
26/04/2015	3064037.63777	0.00047	354182.91115	0.00054	2106.49761	0.00204
Delta	−1.76104	0.0007	−0.25303	0.00083	1.13944	0.00312

The uncertainty of each component, expressed in terms of root mean square (RMS) error, is also included. The RMS Delta is calculated with the error propagation, assuming that the covariance terms equal zero

frequency noise. In addition, in this case, the Pearson coefficient is low with values between 0.09 and 0.16. As a consequence, the E–W component, that showed a smoother displacement with respect to the step-like deformation which occurred in the N–S component, could not be due to delays in the GNSS time arrival due, for example, to local changes in the atmospheric conditions.

A summary of the observed coseismic displacements derived from the GNSS data is reported in Table 2.

A solution to the problem of finding the superficial coseismic displacements given a finite rectangular fault in a homogeneous elastic half space was given in 1985 by Okada. This solution is of great interest to seismologists and geodesists, because exploiting the superposition principle even a very complicated rupture process could be simulated. The Okada model (Okada 1985) has been successfully applied to various earthquakes, leading to a better comprehension of the rupture mechanics (e.g., Toda et al. 1998; Caporali et al. 2005). It was also implemented in several inversion (Battaglia et al. 2013; Cheloni et al. 2010) schemes to retrieve the slip which occurred on fault given the observed static displacements.

In our contribution, we used the software Coloumb3 (Toda et al. 2011), distributed by the USGS to construct the fault model, discretized into patches, and to calculate the surface displacements according to the Okada (1985) equations. We test two fault models: one from the USGS, which was derived from only seismological data and the other from Galetzka et al. (2015) which included continuous

GPS and InSAR data in a joint inversion approach. In both cases, the fault model considers an area of about 200 km × 150 km; however, most of the slip occurred in a narrower area of about 150 km × 50 km located in the deeper section of the Main Himalayan Thrust. According to both the inverted models, the slip has not involved the most superficial section of the fault which is locked, as also pointed out by other authors (Mencin et al. 2016).

Both the models reveal a similar strike and dip of the fault: the most evident differences are in the slip magnitude distribution in each patch in which the fault has been discretized.

Figure 3 presents the comparison between the observed data and the modelled values using the fault model from Galetzka et al. (2015). In addition to our stations NAGA and PYRA, we include also the GNSS stations of the UNAVCO project that were used in the study of Galetzka. The stations NAGA and PYRA had not been used by Galetzka et al. (2015). The slip on fault according to Galetzka et al. (2015) is illustrated with the contour representation. In general, the fitting is quite good, especially in terms of direction of movement. The calculated magnitude of the displacement in the NAGA station seems to be a little underestimated, confirming the underestimation of the other two near-fault stations. Changing the fault parameters, such as varying the values of the halfspace rigidity or slightly changing the dip and strike angles, does not increase the fit. For instance, varying the dip angle, from 9 to 7 degrees, increases the fit in the horizontal plane, but at the same time, the vertical component fit is worsened. In the following chapter, an equivalent uniform slip
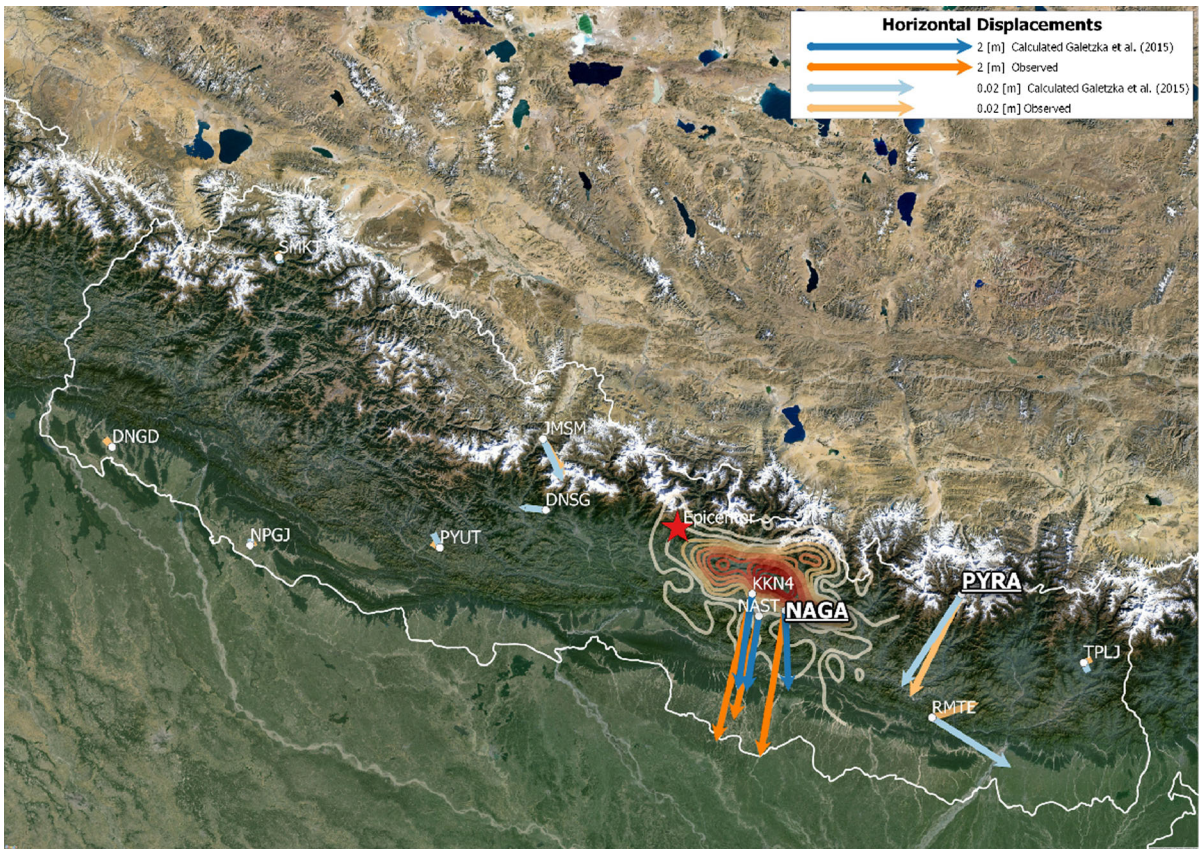
Figure 3
Observed (*orange/light orange*) and modelled (*blue/light blue*) horizontal coseismic displacements in our stations PYRA and NAGA and in the other stations used by Galetzka et al. (2015). The fault model, used for the calculations, is reported with the contours of equal slip: the maximum slip occurred is 5.77 m. The location of the epicenter of 7.8 M_w is plotted with a *red star*
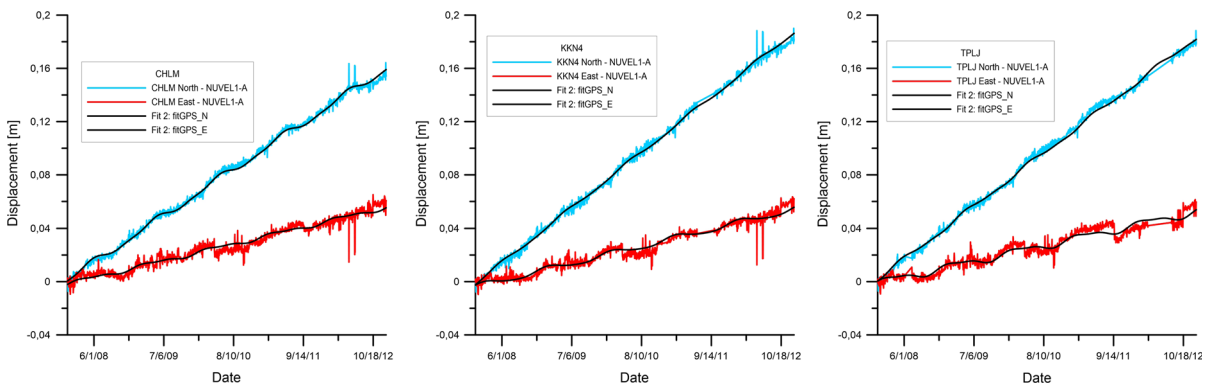

Figure 4
5-year time series of the stations CHLM, KKN4, and TPLJ: cyan lines are the North component, while red the East. From all models, the velocity model NUVEL1-A (DeMets et al. 1990, 1994) has been subtracted. The *black lines* are the fitted linear and periodic components according to Eq. 2

model is used to improve the fit by changing the width of the fault.

The USGS solution (2016) on the other hand fits the data worse with respect to the Galetzka et al. (2015) model; the predicted surface displacements are too small in terms of magnitude.

Regarding NAGA station, the USGS solution (2016) is able to explain less than 50% of the observed magnitude, while the Galetzka et al. (2015) model reproduces the magnitudes to almost 60% of the observed signal. The PYRA station shows a better fit with Galetzka et al. (2015) model, with a perfect match between observed and modelled displacements.

An explanation of the discrepancy in the NAGA station could be that Galzetka et al. (2015) invert for the slip occurred on fault using GPS and InSAR interferometry data; interferometry data usually are a smoothed representation of the observed displacements, so locally, discrepancies with GPS data could be present. In the supplementary materials of the article, Galetzka et al. (2015) reported the processing of the InSAR images: the displacement was obtained by repeated observations of the SAR scenes at May 3 and February 22 2015, both on a descending path with 56 m baseline difference. The processing included a 500 m Gaussian low-pass filter to improve the coherence. The final superficial deformation according to InSAR interferometry data shows maximum displacements along Line of Sight of only 1.1–1.2 m against 1.7 m that we have found for NAGA, the almost 1.8 m in NAST, and 1.3 m in KKN4. The model underestimates the InSAR observations in the area, where the stations NAGA and KKN4 are located, as shown in the supplementary materials (Galetzka et al. 2015). The PYRA station on the other hand showed an almost perfect fit in terms of both magnitude and direction of the movement with the modelled coseismic deformation.

From the slip on the fault, we evaluate an average strain released by the earthquake from the formula:

$$\varepsilon = \Delta u / L. \tag{1}$$

where ε is the shear strain along slip direction, Δu is the average slip, and L corresponds in our case to the width of the fault along dip (50 km), since the slip occurred prevalently as a thrust movement. The

average slip is 3.5 m. Therefore, the released strain by the Gorkha earthquake amounts to about 7×10^{-5} strain.

4. Long Period GNSS Time Series: Estimation of the Interseismic Deformation

The time series derived from GNSS data allows us to measure the deformation to which an area is subjected and evaluate its strain rate.

According to the UNAVCO database (2016), the area includes over 20 continuous GPS stations in a 500-km radius around the epicenter and all of them present different time coverages, with some of them recently placed (in the last 2 years). Some stations present also temporal gaps in the acquired time series, in some cases up to 2–3 months. Taking into account these limitations, we selected three stations that guarantee at least 5 years of continuous observation with temporal gaps limited to some days/year. The stations selected were: CHLM, KKN4, and TPLJ.

The elaboration process for these stations was almost the same as for the coseismic time series, presented before, but we used a different double-difference technique, with a daily position for stations. Using a parallel approach with the Bernese software, we calculated stations positions over 5 years, from 2008 to 2012 in a fast high precision procedure.

The time series of these four stations are plotted in Fig. 4. The stations CHLM, KKN4, and TPLJ show a coherent North-East secular trend in which different periodic signals are superposed. The periodicities were estimated by spectral analysis. We find that all the stations are subject to yearly and semi-annual periodicities connected to temperature variations and hydrological effects. Multiannual oscillations, centered at the frequency 0.6 1/year, are also evident in the east/west and up/down components. Detailed analysis on the hydrological effects in the Himalaya and their implications in the recovery of the tectonic motions are discussed in Fu and Freymueller (2012). Interestingly, in the Up and East components, pluriannual oscillations appear. To correctly estimate the secular trend at each station, it is important to isolate the yearly and semi-annual oscillations from the
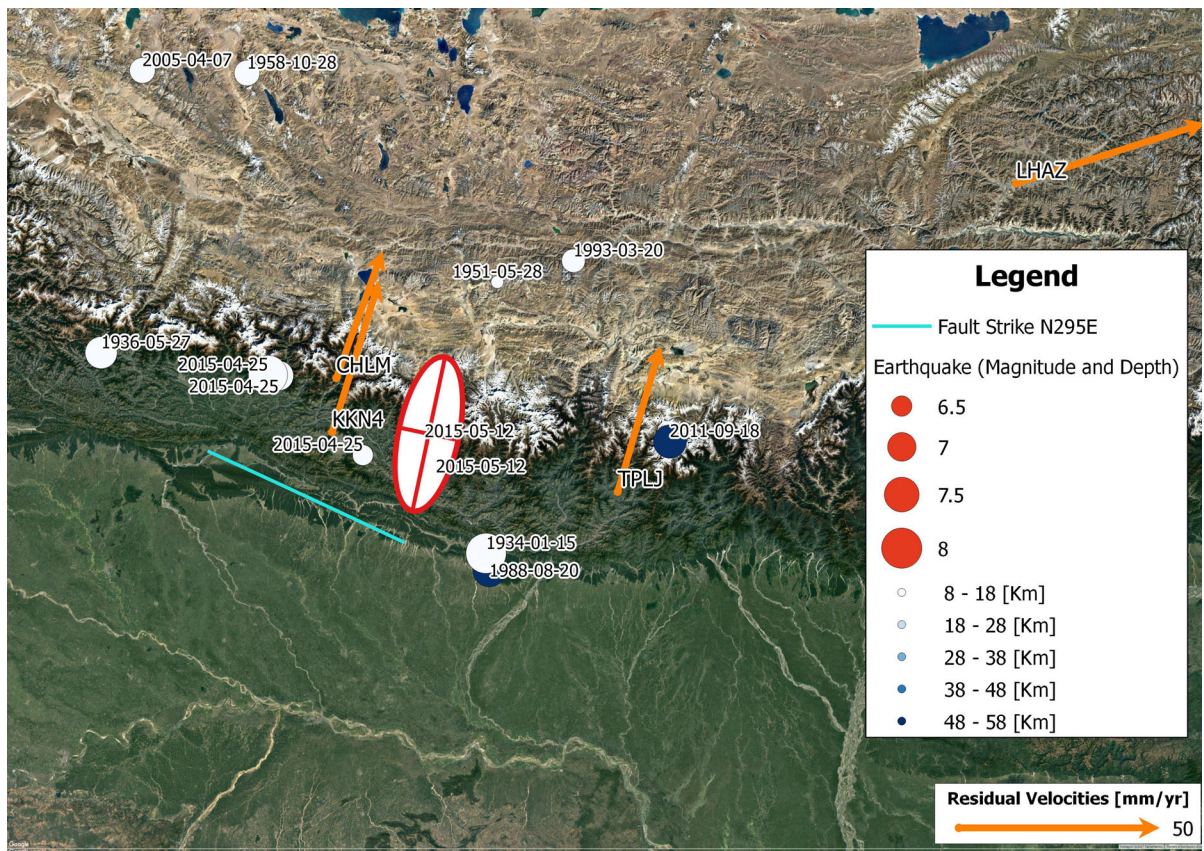
Figure 5
Vectors show the velocity residuals, with respect to EURA plate (NUVEL1-A model). The strain rate ellipse is reported together with the principal axes. Earthquakes from the USGS catalogue in the past 100 years are shown with circles: size is proportional to magnitude, and colors report the hypocenter depth (*white* is shallow earthquake)

GNSS data series. We adopt a widely used approach (Ader et al. 2012) that fits the GNSS time series through the following relation and efficiently recovers the linear trend:

$$x(t) = k + mt + \text{Acos}\left(\frac{\pi}{Ta}t\right) + \text{Bcos}\left(\frac{\pi}{Ta}t\right)$$
$$+ \text{Ccos}\left(\frac{2\pi}{Ta}t\right) + \text{Dcos}\left(\frac{2\pi}{Ta}t\right) \qquad (2)$$

where m is the secular trend, A and B are the annual amplitude oscillations, and C and D are the semi-annual components. The parameters are easily calculated through a least squares regression. We did not take advantage of GRACE data for removing the seasonal deformation transients from our GNSS time series, as proposed by other authors (Fu et al. 2012), because the resolution of GRACE data is not

adequate to recover possible local variations in the response to hydrologic loads in our GNSS stations configuration. As shown in Devoti et al. (2015), the hydrologic effects are local, at much smaller scale than the 300-km resolution of GRACE, especially in mountain areas.

The three stations show an impressive 35 mm/year movement in the N15°E direction, as evident from Fig. 5. In this figure, we include also the LHAZ station that shows a more pronounced eastward movement, indicating that the station is located on the Eurasia plate and subjected to the eastern extrusion of crustal material (Shin et al. 2015). Obviously, the relative movement between this station and the other 3 is accommodated by the thrusts at the feet of the Himalayan chain and is the cause of the high

seismic activity of the region, as demonstrated also by the Gorkha earthquake.

From the velocity field, we could estimate the interseismic strain rate for the area. Using the approach of Shen et al. (1996), we calculated an average strain rate of the area. The method relies on a least squares approach to interpolate the strain variations in a regular grid, given the velocity observations of the GNSS network. In our case, spatial variations of the strain rate could not be estimated, due to the scarcity of GNSS long-term observations of the Nepalese network.

The strain rate is reported in Fig. 5 with the ellipse that shows the maximum axis of deformation: the maximum axis of compression is oriented N15°E with magnitude 132 nanostrain/year, while the minor axis is a dilatation with modulus 2 nanostrain/year. The maximum axis is almost perfectly perpendicular to the strike of Gorkha's fault. The spatial configuration of the GNSS network indicates that the calculated strain rate is representative for an area located 90-km northward of the fault trace in the direction perpendicular to the strike.

To validate our estimate of the strain rate, that is important for recurrence time calculation, we implement a simple fault model (Savage 1983) apt to describe subduction events. In this model, the subducting plate on average moves into the asthenosphere relative to the overriding plate with the same speed of the relative convergence rate of the two plates. The subduction process is divided into a locked upper zone, from the surface to about 40-km depth, and a steadily sliding zone from below and reaching greater depths. The locked zone moves in a stick slip movement, with times of non-sliding interseismic phase, and a sudden rupture at the earthquake occurrence. The earthquake down-dip slip according to this model equals to the horizontal convergence rate multiplied by the time between successive ruptures. The strain at surface assimilates a sawtooth, as it starts at zero after the rupture, increasing linearly to a maximal value at rupture, with constant strain rate during an interseismic cycle. The measured strain and strain rate are modulated by a nonlinear dependence of the position relative to the fault, with maximum horizontal compression just above the mid-line of the fault, and the smallest

values in correspondence with the projection of top and bottom of the locked fault. It is of interest to investigate the consistency of the modelled fault, the near-fault strain rate, the amount of down-dip fault slip, the convergence rate, and the rupture recurrence times in the frame of this model. Based on the Savage (1983) model, the following relations should hold.

With u = down-dip slip with rupture (m), T = recurrence time of earthquake on fault (year), B = plate convergence rate (m/year), it should hold:

$$u = BT. \tag{3}$$

The strain rate ε_{xx} as a function of the position perpendicular to the strike (x) is modelled in Savage(1983) by the equation:

$$\varepsilon_{xx} = \frac{2BT}{\pi} s \sin\alpha(s - x\cos\alpha)(x - s\cos\alpha)/D^4 \tag{4}$$

where s is the surface width, α is the dip angle, and $D^2 = x^2 + s^2 - 2xs\cos\alpha$.

From Eq. 4, the strain rate is easily calculated:

$$\dot{\varepsilon}_{xx} = \frac{2B}{\pi} s \sin\alpha(s - x\cos\alpha)(x - s\cos\alpha)/D^4. \tag{5}$$

Setting the parameters of the Gorkha earthquake into Eq. 4, $\alpha = 11°$, $s = 50$ km and assuming $B = 20$ mm/year, as reported in Mencin et al. (2016), we could compare the strain rate calculated from the three GNSS time series and the outcome from the model. Figure 6 shows the strain rate variations according to Savage (1983) along a profile perpendicular to the fault trace (0 m corresponds to fault plane intersecting topographic surface); the red line reports the 132 nanostrain/year estimated for our stations. The intersection of this line with the modelled strain rate occurs at different positions along the profile; an intersection is found at around 70 km, slightly in a southern position with respect to our GNSS estimates (90 km). This means that the measured strain rate is too big for a position of 90-km distance, and it would be correct for a position at 70-km distance. This is coherent to the previous observation that the dislocation model underestimates the observed deformation.

Recovering spatial variations in the strain rate would be interesting in the light of the validation of the above-mentioned model. However, up to now, an
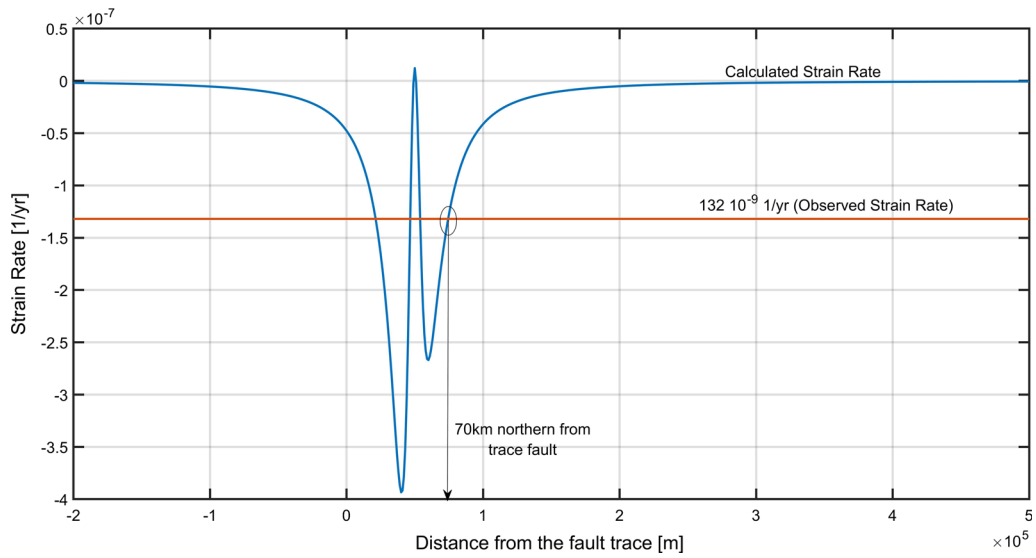
Figure 6
Calculated strain rate profile perpendicular to the fault trace (*blue line*), according to Savage (1983). The observed strain rate is reported with the *red horizontal line*. The intersection occurs at 70 km, while the observed strain rate is located 90-km northward from the fault trace
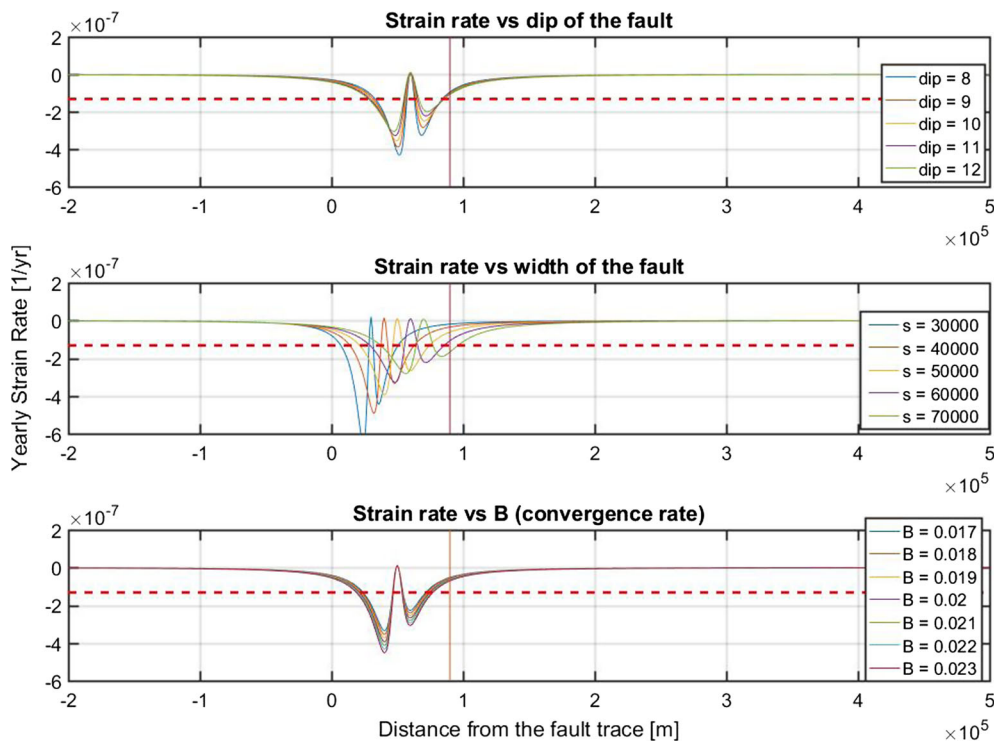

Figure 7
Sensitivity analysis of strain rate in function of dip (°), width (s, in m) of the fault, and plate convergence rate (B, in m/year)

adequate GNSS data set, in terms of spatial and temporal resolutions, is lacking for the Gorkha area. Some new stations have been placed in the Northern and Southern portions of the fault for monitoring the subsequent post-seismic events (Mencin et al. 2016); however, the data could not be used for long-term estimates of the tectonic trends. Considering the GNSS configuration used in the study, we could only make some rough estimates of the errors, with a sensitivity analysis.

Figure 7 shows various strain rate profiles as a function of the dip of the fault, the width, and the convergence rate; the red dashed line is the 132 nanostrain/year level estimated in our GNSS network and the vertical line reports the 90-km distance between the estimated strain rate location and the trace of the fault.

It appears that the width of the fault seems to be a critical parameter, while the other parameters show less influence. At the end considering a fault that is 60-km wide instead of 50 km, a better fit of the observed strain rate is obtained.

The sensitivity analysis proves that our strain rate measurement is compatible with the Gorkha fault model presented and with a convergence rate for the India-Himalaya (B) that amounts to 20 mm/year.

From the average slip occurred on the fault, we could estimate a recurrence time according to the Savage model of 235 year.

In Fig. 5, we plot together with the strain ellipse from our analysis, the fault trace, and the historical seismicity ($M_w > 6.5$) from the USGS database. The fault trace extends over the length marked by the 2015 aftershock sequence. The area was not active in the past 100 years: earthquakes occurred in neighboring segments of the subducting plate. In 1934–1936 both segments, west and east of the 2015 rupture broke with M_w 8 (east, 1934) and M_w 7 (west, 1936) earthquakes. The eastward fault broke again in 1988 with a smaller and deeper event (M_w 6.5). The 2015 sequence broke the segment joining these two faults.

Thapa and Guoxin (2013) compiled a catalogue of the historical seismicity of the whole Nepal: concerning the Gorkha area, they found that it was struck by four >7.5 M_s events in 1255, 1408, 1681, and 1810. Such data appear to be consistent with our estimates from strain rate analysis. Ader et al. (2012) also estimate the recurrence time in the whole Himalaya chain. Taking advantage of the Savage model (1983), they calculate the slip deficit occurring along the Himalayan thrust and consequently the moment deficiency. The authors used Molnar (1979) relation to predict, for the whole Himalayan chain, an average 50-year recurrence for $M_w = 8$. The discrepancy with our estimate could be explained by the different areas considered in the study: our analysis focuses on a specific seismogenic structure which
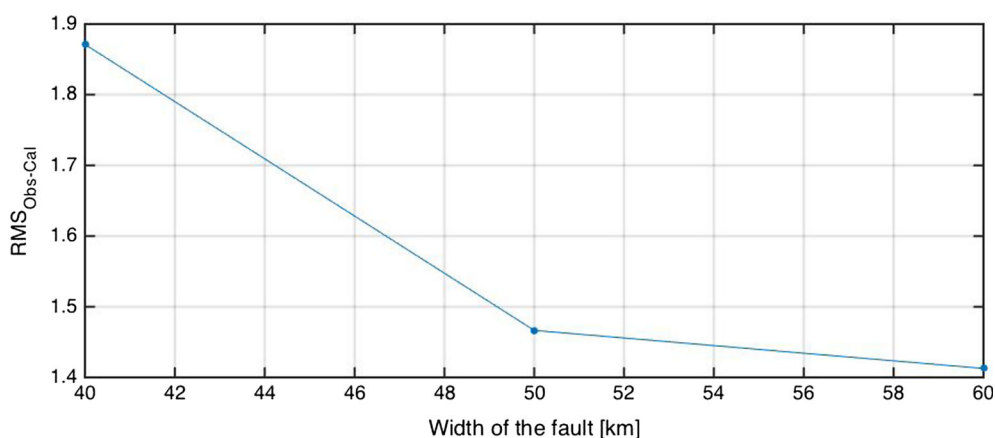

Figure 8
Root mean square residual (m) between observed and calculated displacements summed for all stations as a function of the width of the fault. Increasing the width from 50 to 60 km leads to a slightly better accordance with observed displacement field

caused the Gorkha earthquake, while Ader et al. (2012) conducted a large scale study, giving repeat times for the entire Himalayan arch.

However, we remark that an improvement of the strain rate estimate will be possible in the future by considering the GNSS stations located around the fault that were placed just immediately after the earthquake (Gualandi et al. 2016; Mencin et al. 2016).

We test whether a wider fault gives a better fit also to the GNSS coseismic movement. The above finding regarding the strain rate would suggest that the near-fault observations are better explained by a fault that is 10 km wider than the present model. We compute displacement for an equivalent model, with a homogeneous fault slip, keeping the other fault parameters, such as strike, dip, and rake, the same as the previously used model. In Fig. 8, the root mean square (RMS) error between observed and calculated displacements for different widths of the fault is reported. A decrease in error is seen as the fault width slightly increases from 40 to 60 km.

5. Conclusions

In this contribution, we analyzed the GNSS coseismic signal due to the catastrophic 7.8 M_w Gorkha earthquake which occurred on 25th April 2015. Two GNSS stations were added to the geodetic network present in the area that is available from the UNAVCO database. The NAGA station increases the amount of strong-motion near-fault stations, allowing a robust estimate of the coseismic displacement. The NAGA station confirms that the present earthquake rupture model underestimates the strong-motion dislocation, calling for a coseismic slip on a slightly wider fault. Both these two stations PYRA and NAGA displayed a coseismic offset due to the fault movement. The PYRA station, located next to the Pyramid observatory on Everest, showed signals close to the noise level of GNSS observations. However, a first comparison with meteorological data excluded the effect of a change in the weather conditions in the observed displacements. Hence, we verified the compatibility of the observed

deformation field with the modelled displacement field calculated using the Okada approach. Two fault solutions have been tested: a major concordance is found for the Galetzka et al. 2015 model that exploits also geodetic data, with respect to the only seismological solution of the USGS. Some differences in terms of magnitude between observed and modelled data are present too: it seems that the predicted movement is a little underestimated for the strong-motion near-fault stations. This effect could be explained by the fact that the model had used the InSAR interferometry data in the inversion scheme that could smooth the retrieved slip on the fault.

From the slip on the fault, we derived the shear strain released by the earthquake. The processing of long period data from other GNSS stations located in the area allowed us to estimate the strain rate to which the area is subjected and compare it with the predictions of a model that describes the yearly accumulation of strain due to a locked fault (Savage 1983). Since the GNSS network for the Gorkha area includes only few stations, spatial variations of the strain rate could not be retrieved. However, the estimates of the model are in accordance with the Gorkha fault parameters and the yearly convergence rate, except that for the coseismic observations, the width of the fault should be a bit greater. From the convergence rate, we established a recurrence time of about 235 years.

The comparison with the recurrence time of similar earthquakes in the area, derived from seismological catalogues and historical seismicity, let us infers that the recurrence time of the earthquake from geodetic analysis is realistic. Better estimates of the strain accumulation and release, and retrieving the local spatial variation of the strain rate could only be possible if a dense and continuous geodetic network is established and maintained in the Gorkha area and extended also to the Indian region.

meteorological data. We acknowledge the UNAVCO consortium for the GNSS data of the stations KIT3, KKN4, LAHZ, TPLJ, and CHLM. The reviewers are kindly acknowledged for their fruitful comments that contributed in improving the quality of the paper.

REFERENCES

Ader, T., Avouac, J.-P., Liu-Zeng, J., Lyon-Caen, H., Bollinger, L., Galetzka, J., et al. (2012). Convergence rate across the Nepal Himalaya and interseismic coupling on the Main Himalayan Thrust: implications for seismic hazard. *Journal of Geophysical Research, 117,* B04403. doi:10.1029/2011JB009071.

Arora, B. R., Bansal, B. K., Prajapati, S. K., Sutur, A. K., & Nayak, S. (2017). Seismotectonics and seismogenesis of M_w 7.8 Gorkha Earthquake and its Aftershocks. *Journal of Asian Earth Sciences, 133,* 2–11. doi:10.1016/j.jseaes.2016.07.018.

Avouac, J.-P., Meng, L., Wei, S., Wang, T., & Ampuero, J.-P. (2015). Lower edge of locked main Himalayan thrust unzipped by the 2015 Gorkha earthquake. *Nature Geoscience, 8,* 708–711. doi:10.1038/ngeo2518.Battaglia.

Battaglia, M., Cervelli, P. F., & Murray, J. R. (2013). dMODELS: a MATLAB software package for modeling crustal deformation near active faults and volcanic centers. *Journal of Volcanology and Geothermal Research, 254,* 1–4.

Böhm, J., Werl, B., & Schuh, H. (2006). Troposphere mapping functions for GPS and very long baseline interferometry from European Centre for Medium-Range Weather Forecasts operational analysis data. *Journal of Geophysical Research: Solid Earth, 111,* B02406. doi:10.1029/2005JB003629.

Caporali, A., Braitenberg, C., & Massironi, M. (2005). Geodetic and hydrological aspects of the Merano earthquake of 17 July 2001. *Journal of Geodynamics, 39,* 317–336.

Chaulagain, H., Rodrigues, H., Silva, V., Spacone, E., & Varum, H. (2015). Seismic risk assessment and hazard mapping in Nepal. *Natural Hazards, 78*(1), 583. doi:10.1007/s11069-015-1734-6.

Cheloni, D., D'Agostino, N., D'Anastasio, E., Avallone, A., Mantenuto, S., Giuliani, R., et al. (2010). Coseismic and initial post-seismic slip of the 2009 M_w 6.3 L'Aquila earthquake, Italy, from GPS measurements. *Geophysical Journal International, 181*(3), 1539–1546.

DeMets, C., Gordon, R. G., Argus, D. F., & Stein, S. (1990). Current plate motions. *Geophysical Journal International, 101,* 425–478.

DeMets, C., Gordon, R. G., Argus, D. F., & Stein, S. (1994). Effect of the recent revisions to the geomagnetic reversal timescale. *Geophysical Research Letters, 21,* 2191–2194.

Denolle, M. A., Fan, W., & Shearer, P. M. (2015). Dynamics of the 2015 *M* 7.8 Nepal earthquake. *Geophysical Research Letters, 42,* 7467–7475. doi:10.1002/2015GL065336.

Devoti, R., Zuliani, D., Braitenberg, C., Fabris, P., & Grillo, B. (2015). Hydrologically induced slope deformations detected by GPS and clinometric surveys in the Cansiglio Plateau, Southern Alps. *Earth and Planetary Science Letters, 419,* 134–142.

Fan, W., & Shearer, P. M. (2015). Detailed rupture imaging of the 25 April 2015 Nepal earthquake using teleseismic P waves. *Geophysical Research Letters, 42,* 5744–5752.

Fu, Y., & Freymueller, J. T. (2012). Seasonal and long-term vertical deformation in the Nepal Himalaya constrained by GPS and GRACE measurements. *Journal of Geophysical Research, 117,* B03407. doi:10.1029/2011JB008925.

Fu, Y., Freymueller, J. T., & Jensen, T. (2012). Seasonal hydrological loading in southern Alaska observed by GPS and GRACE. *Geophysical Research Letters, 39,* L15310. doi:10.1029/2012GL052453.

Galetzka, J., Melgar, D., Genrich, J. F., Geng, J., Owen, S., Lindsey, E. O., et al. (2015). Slip pulse and resonance of the Kathmandu Basin during the 2015 Gorkha earthquake, Nepal. *Science, 349,* 1091–1095.

Grandin, R., Vallée, M., Satriano, C., Lacassin, R., Klinger, Y., Simoes, M., et al. (2015). Rupture process of the $M_w = 7.9$ 2015 Gorkha earthquake (Nepal): insights into Himalayan megathrust segmentation. *Geophysical Research Letters, 42,* 8373–8382.

Gualandi, A., Avouac, J-P., Galetzka, J., Genrich, J.F., Blewitt, G., Adhikari,L.B., Koirala, B.P., Gupta, R., Upreti, B.N., Pratt-Sitaula, B., Liu-Zeng, J. (2016). Pre- and post- seismic deformation related to the 2015, M_w7.8 Gorkha earthquake, Nepal, *Tectonophysics*, in press, doi:10.1016/j.tecto.2016.06.014.

Mencin, D., Bendick, R., Upreti, B. N., Adhikari, D. P., Gajurel, A. P., Bhattarai, R.R., Shrestha, H.R., Bhattarai, T. N., Mananadhar, N., Galetzka, J., Knappe, E., Pratt-Sitaula, B., Aoudia, A., Bilham, R. (2016). Himalayan strain reservoir inferred from limited afterslip following the Gorkha earthquake, Nature Geoscience, 9, 533-537, doi:10.1038/ngeo2734.

Molnar, P. (1979). Earthquake recurrence intervals and plate tectonics. *Bulletin of the Seismological Society of America, 29,* 211–229.

Okada, Y. (1985). Surface deformations due to shear and tensile faults in a halfspace. *Bull. Seism. Soc. Am., 75*(4), 1135–1154.

Rajendran, K., & Rajendran, C. P. (2011). Revisiting the earthquake sources in the Himalaya: perspectives on past seismicity. *Tectonophysics, 504*(1–4), 75–88.

Savage, J. C. (1983). A dislocation model of strain accumulation and release at a subduction zone. *Journal of Geophysical Research, 88,* 4984–4996.

Shen, Z.-K., Jackson, D. D., & Ge, B. X. (1996). Crustal deformation across and beyond the Los Angeles basin from geodetic measurements. *Journal of Geophysical Research, 101*(B12), 27957–27980.

Shin, Y. H., Shum, C. K., Braitenberg, C., Lee, S. M., Na, S.-H., Choi, K. S., et al. (2015). Moho topography, ranges and folds of Tibet by analysis of global gravity models and GOCE data. *Scientific Reports, 5,* 1–7. doi:10.1038/srep11681.

Sreejith, K. M., Sunil, P. S., Agrawal, R., Saji, A. P., Ramesh, D. S., & Rajawat, A. S. (2016). Coseismic and early postseismic deformation due to the 25 April 2015, M_w 7.8 Gorkha, Nepal, earthquake form InSAR and GPS measurements. *Geophysical Research Letters, 43,* 3160–3168.

Thapa, D. R., & Guoxin, W. (2013). Probabilistic seismic hazard analysis in Nepal. *Earthquake Engineering and Engineering Vibration, 12,* 577–586.

Toda, S., Stein, R.S., Reasenberg, P.A., Dieterich, J.H. (1998). Stress transferred by the $M_w = 65$ Kobe, Japan, shock: Effect on aftershocks and future earthquake probabilities. J Geophys Res 103(24), 543–24,565.

Toda, S., Stein, R.S., Sevilgen, V., Lin, J. (2011). Coulomb 3.3 Graphic-rich deformation and stress-change software for earthquake, tectonic, and volcano research and teaching—user guide. U.S. Geological Survey Open-File Report. http://pubs.usgs.gov/of/2011/1060/. Accessed 10 Dec 2016.

UNAVCO (2016) ftp://data-out.unavco.org/pub/rinex, http://www.unavco.org/data/gps-gnss/data-access-methods/dai2/app/dai2.html#. Accessed 10 Dec 2016.

USGS. (2016). Event page M7.8–36 km E of Khudi, Nepal. https://earthquake.usgs.gov/earthquakes/eventpage/us20002926#executive. Accessed 10 Dec 2016.

Wang, K., & Fialko, Y. (2015). Slip model of the 2015 M_w 7.8 Gorkha (Nepal) earthquake from inversions of ALOS-2 and GPS data. *Geophysical Research Letters, 42,* 7452–7458.